Utilizing strongly absorbing materials for low-loss surface-wave nonlinear optics

Nicolai B. Grosse, Philipp Franz, Jan Heckmann, Karsten Pufahl, and Ulrike Woggon
Institut für Optik und Atomare Physik, Technische Universität Berlin, Straße des 17. Juni 135, 10623 Berlin, Germany

(Received 3 October 2017; published 18 April 2018)

Optical media endowed with large nonlinear susceptibilities are highly prized for their employment in frequency conversion and the generation of nonclassical states of light. Although the presence of an optical resonance can greatly increase the nonlinear response (e.g., in epsilon-near-zero materials), the non-negligible increase in linear absorption often precludes the application of such materials in nonlinear optics. Absorbing materials prepared as thin films, however, can support a low-loss surface wave: the long-range surface exciton polariton (LRSEP). Its propagation lifetime increases with greater intrinsic absorption and reduced film thickness, provided that the film is embedded in a transparent medium (symmetric cladding). We explore LRSEP propagation in a molybdenum film by way of a prism-coupling configuration. Our observations show that excitation of the LRSEP mode leads to a dramatic increase in the yield of second-harmonic generation. This implies that the LRSEP mode is an effective vehicle for utilizing the nonlinear response of absorbing materials.

DOI: 10.1103/PhysRevA.97.043844

I. INTRODUCTION

Aside from their applications as color filters or saturable absorbers, intrinsically absorbing materials are seldom considered as optical elements. In bulk form, attenuation accompanies any effort to guide or focus light. Considering transparency as a requisite for efficiently converting optical frequencies, absorbing materials are typically avoided as nonlinear media. Yet, here is an opportunity missed, because as the probing frequency approaches an absorption resonance, the nonlinear susceptibility of a material can greatly exceed those values found off-resonance [1–5].

To employ absorbing materials as nonlinear optical media, one needs to find a way to have light interacting with the medium over a long propagation distance, i.e., polarizing it over many wave cycles, but without the associated absorption. An important discovery was that intrinsically absorbing materials can sustain low-loss surface waves [6], whose associated quasiparticles are conventionally termed long-range surface exciton polaritons (LRSEPs) [7]. Provided that the configuration is chosen to be a film of absorbing material that is embedded in a transparent medium, the propagation length of LRSEP waves becomes arbitrarily long in the limit of vanishing film thickness. The phenomenon requires only that the material's permittivity be predominantly imaginary over that particular range of optical frequencies. Hence it is not only semiconductors, but also the transition metals, metal oxides, and dichalcogenides that can support LRSEP, whose linear propagation properties having been confirmed from the ultraviolet to the infrared [8–19].

However, the most compelling aspect of absorbing materials—their nonlinear optical response—have not, to our knowledge, been studied in the context of LRSEP. Questions remain open regarding the overall effective nonlinearity that the system can attain. This performance will likely depend on the level of field enhancement, the propagation length, the accessible elements of the nonlinear susceptibility tensor, phase matching between the relevant modes, and efficient coupling to the far field. Understanding these factors will be the key to propelling absorbing materials into applications such as electro-optic modulation and frequency conversion.

In this work, we present experimental observations of a 25-fold increase in second-harmonic yield due to the excitation of LRSEPs in a film of strongly absorbing material. Our analysis indicates that LRSEPs not only create a local field enhancement at the fundamental frequency (thus driving the nonlinear response), but also facilitate a vast increase in the nonlinear interaction length compared with simple reflection. The molybdenum (Mo) in this study has a permittivity dominated by its imaginary part in the near infrared. Although being a conductor, Mo is pushed out of the plasmonic regime in the near infrared by a set of strong optical transitions in the visible. Since it is known that weak transitions leading to the epsilon-near-zero (ENZ) conditions of materials can be accompanied by extraordinary nonlinear susceptibilities [20], strong transitions can be expected to excel in this regard.

Our results confirm that strongly absorbing films are essentially transparent to LRSEPs and guide them, yet they allow a nonlinear interaction with the material which leads to the emission of second-harmonic radiation. The demonstration of this phenomenon in Mo suggests that intrinsically absorbing materials, in general, can be approached as an alternative to conventional transparent media for the desired properties of second-order and third-order nonlinear susceptibility.

II. THEORETICAL DESCRIPTION

It is instructive to break down the phenomenon of second-harmonic generation (SHG) in this system into several steps: (i) the field and propagation characteristics of the LRSEP mode, (ii) the excitation of this mode by an evanescent plane wave via the coupling prism, (iii) the subsequent second-order polarization, and (iv) how this nonlinear source becomes a propagating second-harmonic wave that radiates out to the far field via the prism.

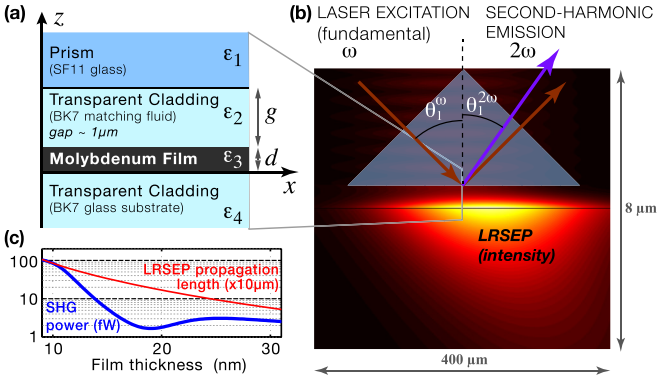

FIG. 1. (a) Absorbing film (molybdenum) is embedded in symmetric transparent cladding. (b) The Otto prism-coupling configuration is used to illuminate the LRSEP mode, while the second harmonic (SHG) is detected in the far field. (c) LRSEP propagation length and SHG power over film thickness. Model used constant fundamental input intensity, but gap adjusted to ensure critical coupling.

A. Mode analysis

We describe the system as consisting of four layers of isotropic nonscattering optical media labeled $i = \{1,2,3,4\}$ that are stacked on top of each other in the z direction, see Figs. 1(a) and 1(b), moving, respectively, from the coupling prism ($i=1$; $g+d<z<\infty$), to index matching fluid ($i=2$; $d<z<g+d$), to the absorbing film ($i=3$; $0<z<d$), and ending with the glass substrate ($i=4$; $-\infty<z<0$). The optical response of each material is described by its complex dielectric function $\epsilon_i(\omega)$, where ω is the optical frequency related to the wavelength $\lambda_0 = 2\pi c/\omega$ and wave vector $k_0 = \omega/c$ of freely propagating light. At the fundamental (ω) and second-harmonic (2ω) frequencies of interest, the absorbing core is assumed to have a complex dielectric function ϵ_3. The cladding is assumed to be symmetric and transparent $\epsilon_2 = \epsilon_4 = |\epsilon_4|$, while the coupling prism is transparent but more optically dense: $\epsilon_1 = |\epsilon_1| > \epsilon_4$.

The aim is to find the complex propagation constant $\beta = \beta_{\mathcal{R}} + i\beta_{\mathcal{I}}$ of the LRSEP mode alone, i.e., for the uncoupled case. In the limit of a large gap ($g \gg \lambda_0$), solutions of β are found by piecing together plane waves in the media $i = \{2,3,4\}$, and solving for the wave vector and amplitudes that fulfill Maxwell's equations [6]. β is thus obtained by finding solutions to

$$\tanh(2i\,k_{3,z}\,d) = -\frac{k_{4,z}/\epsilon_4}{k_{3,z}/\epsilon_3}, \tag{1}$$

where β relates to the z components of the wave vectors via $k_{i,z} = \sqrt{\epsilon_i k_0^2 - \beta^2}$. The propagation length of the mode is $L = 2\pi/2\beta_{\mathcal{I}}$, while $N = \beta_{\mathcal{R}}/2\beta_{\mathcal{I}}$ gives the number of wave cycles propagated until the LRSEP intensity attenuates to $1/e$.

Figure 2(a) shows how β depends on film thickness and core permittivity. The plots are independent of the optical frequency, yet they do depend on the cladding permittivity (glass with ϵ_4=2.274). A cutoff for bound propagation occurs when films are too thick ($\gtrsim$100 nm). As the films become thinner, the mode crosses the light line, becoming bound, while the lifetime increases; also see Fig. 1(c). In the limit of vanishing film thickness, the mode asymptotes toward the light

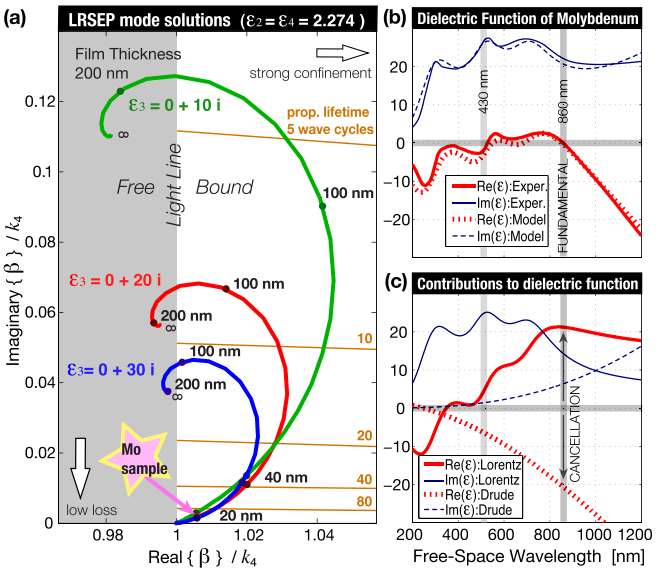

FIG. 2. (a) Solutions for the propagation constant β of the LRSEP mode showing how film thickness and permittivity influence the momentum and propagation lifetime. The former is given by the real part of β, while the latter scales inversely with the imaginary part of β. As a film is made thinner, the solution spirals in towards the limiting case of free-space propagation in the cladding medium. At this point, the property of transverse confinement is completely traded in for lossless propagation. (b) Dielectric function data of Mo and a model fit that incorporates a Drude response together with three Lorentzian oscillators in the visible. (c) The contributions of Drude (plasma) and Lorentz (electronic transitions) in the model are shown separately. At 860 nm those two contributions cancel out for the real part of the dielectric function, thereby leaving only an imaginary part.

line with an unlimited propagation lifetime. For this limiting case, the mode is indistinguishable from that of a plane-wave propagating in the cladding parallel to the interface. However, for reasonable choices of material and film thickness $\epsilon_3 = 22i$ and $d = 19$ nm, one obtains a surface wave that is transversally well confined in the cladding $1/(2\,\mathrm{Im}\{k_{4,z}\}) = 0.44\ \mu$m and lasts $N = 336$ wave cycles over a distance of $L = 191\ \mu$m. A film having greater intrinsic absorption tends to encourage stronger confinement for an equally long propagation lifetime.

B. Far-field excitation and reflection

The task now is to couple light into the LRSEP mode and calculate the reflected intensity in the far field. As such, the coupling gap g is reduced and all media are considered $i = \{1,2,3,4\}$. We consider a p-polarized plane-wave light incident in the xz plane at an angle of θ_1^ω to the normal (within the prism). The plane wave is reflected from each interface with the Fresnel coefficient

$$r_{ij}^\omega = \frac{\epsilon_i^\omega k_{j,z}^\omega - \epsilon_j^\omega k_{i,z}^\omega}{\epsilon_i^\omega k_{j,z}^\omega + \epsilon_j^\omega k_{i,z}^\omega} \tag{2}$$

and transmitted with

$$t_{ij}^\omega = (1 + r_{ij}^\omega)\sqrt{\epsilon_i^\omega/\epsilon_j^\omega}, \tag{3}$$

where $k^{\omega}_{i,z} = [\epsilon^{\omega}_i (k^{\omega}_0)^2 - (k^{\omega}_x)^2]^{1/2}$ are the wave-vector components normal to the interface. These are constrained by the wave-vector component that is parallel to the interface: $k^{\omega}_x = \sqrt{\epsilon^{\omega}_1} k^{\omega}_0 \sin(\theta^{\omega}_1)$ which is identical in all four media, but which we choose to define over the incident angle θ^{ω}_1. The angles in the other are derived using Snell's law of refraction. Using a nested resonator approach, we arrive at the combined amplitude reflectivity $\bar{r}^{\omega}_{14}$ on the side of the coupling prism:

$$\bar{r}^{\omega}_{14} = r^{\omega}_{12} + \frac{t^{\omega}_{12} t^{\omega}_{21} \bar{r}^{\omega}_{24} e^{2i\phi^{\omega}_2}}{1 - r^{\omega}_{21} \bar{r}^{\omega}_{24} e^{2i\phi^{\omega}_2}}, \tag{4}$$

which relies on the resonator reflectivity

$$\bar{r}^{\omega}_{24} = r^{\omega}_{23} + \frac{t^{\omega}_{23} t^{\omega}_{32} r^{\omega}_{34} e^{2i\phi^{\omega}_3}}{1 - r^{\omega}_{32} r^{\omega}_{34} e^{2i\phi^{\omega}_3}} \tag{5}$$

and the phase acquired from propagation, $\phi^{\omega}_2 = k^{\omega}_{2,z} g$ and $\phi^{\omega}_3 = k^{\omega}_{3,z} d$.

The resulting intensity reflectivity $I^{\omega}_{\text{refl}} = |\bar{r}^{\omega}_{14}|^2$ is plotted as a function of incident angle θ^{ω}_1 in Fig. 3(a). Note how the absorption feature, the attenuated total internal reflection (ATR), goes to zero at the angle $\theta_{\text{ATR}} = 59.1^{\circ}$. This is indicative of critical coupling between the LRSEP mode and the far field (for a gap $g = 709$ nm). ATR occurs at an angle beyond total internal reflection (TIR) for the prism-cladding interface ($\theta_{\text{TIR}} = 58.9^{\circ}$), so that the fields involved are evanescent in form. The connection between ATR and LRSEP modes is underscored by evaluating the condition for phase matching between the incident plane wave and the LRSEP mode (i.e., $k_x = \beta_{\mathcal{R}}$). Reexpressing this condition as $\sin(\theta^{\omega}_1) = \beta_{\mathcal{R}}/(k^{\omega}_0 \sqrt{\epsilon^{\omega}_1})$ yields $\theta^{\omega}_1 = 59.4^{\circ}$, which is marked by the arrow in Fig. 3(a). Note that $(\theta^{\omega}_1 - \theta_{\text{ATR}}) = 0.3^{\circ}$, which is a shift in the propagation constant of the LRSEP mode due to radiative damping caused by the coupling prism. Mode parameters can be extracted from ATR data using a Lorentz function fitting procedure [21]. For the case here, radiative damping reduces the LRSEP propagation length from its intrinsic value $N = 336$ to an effective $N_{\text{eff}} = 237$ wave cycles.

C. Second-order polarization

Both the core and cladding materials involved possess inversion symmetry. Hence the presence of a plane-wave field within those media cannot give rise to a second-order polarization. However, at an interface, surface nonlinearities do arise, due to the break in symmetry [22]. In our system, three unique nonlinear susceptibilities are possible: $\chi^{(2)}_{z:zz}$, $\chi^{(2)}_{z:xx}$, and $\chi^{(2)}_{x:xz}$. When field gradients are present within a centrosymmetric medium, a source from the bulk becomes possible. For SHG in film geometries, the contribution from the bulk cannot be isolated from those of the surface terms [23], and we therefore treat the surface nonlinear susceptibilities as effective values.

Our absorbing material of choice was Mo because ellipsometric data [24] show that its permittivity becomes pure imaginary at a wavelength of $\lambda_0 = 860$ nm; see Fig. 2(b). This behavior can be understood as the combined response of a Drude model of conduction-band electrons, together with a set of Lorentzian resonances caused by strong transitions (301 nm, 504 nm, and 725 nm); see Fig. 2(c). Despite being a conductor, the overall linear optical response of Mo at this wavelength is dominated by the transitions leading to $\epsilon^{\omega}_3 \approx 0 + 22i$. The application of a strict hydrodynamic model for the conduction electrons to describe the linear and nonlinear optical response would not be appropriate. In this work we use a phenomenological model of surface SHG based on calculations of the fundamental field at the interfaces. Although the model cannot predict absolute harmonic yields, it describes the role of the fundamental LRSEP field, and the outcoupling efficiencies and interference of the second-harmonic sources.

The bulk and surface nonlinear responses of the transparent media (substrate, matching fluid, and prism) are negligible in comparison to Mo (see Results section for evidence). Henceforth, we only consider the surface nonlinear susceptibilities of the Mo film which are driven by the upward ↑ and downward ↓ propagating fundamental waves that are within the Mo medium located at the boundaries $z = 0^+$ (bottom) and $z = d^-$ (top). The fields obtained via a Fabry-Pérot method are

$$E^{\omega}_{\downarrow 3}(d^-) = E^{\omega}_{\downarrow 1} \frac{\bar{t}^{\omega}_{13}}{1 - \bar{r}^{\omega}_{31} r^{\omega}_{34} e^{2i\phi^{\omega}_3}}, \tag{6}$$

$$E^{\omega}_{\uparrow 3}(d^-) = E^{\omega}_{\downarrow 3}(d^-)\, r^{\omega}_{34}\, e^{2i\phi^{\omega}_3}, \tag{7}$$

$$E^{\omega}_{\downarrow 3}(0^+) = E^{\omega}_{\downarrow 3}(d^-)\, e^{i\phi^{\omega}_3}, \tag{8}$$

$$E^{\omega}_{\uparrow 3}(0^+) = E^{\omega}_{\downarrow 3}(d^-)\, r^{\omega}_{34}\, e^{i\phi^{\omega}_3}, \tag{9}$$

where these rely on the resonator responses:

$$\bar{t}^{\omega}_{13} = \frac{t^{\omega}_{12} t^{\omega}_{23} e^{i\phi^{\omega}_2}}{1 - r^{\omega}_{21} r^{\omega}_{23} e^{2i\phi^{\omega}_2}}, \tag{10}$$

$$\bar{r}^{\omega}_{31} = r^{\omega}_{32} + \frac{t^{\omega}_{23} t^{\omega}_{32} r^{\omega}_{21} e^{2i\phi^{\omega}_2}}{1 - r^{\omega}_{23} r^{\omega}_{21} e^{2i\phi^{\omega}_2}}. \tag{11}$$

The combined fields are analyzed into their vectorial components:

$$E^{\omega}_{3,x}(z) = \left[E^{\omega}_{\downarrow 3}(z) - E^{\omega}_{\uparrow 3}(z)\right] \cos(\theta^{\omega}_3), \tag{12}$$

$$E^{\omega}_{3,z}(z) = \left[E^{\omega}_{\downarrow 3}(z) + E^{\omega}_{\uparrow 3}(z)\right] \sin(\theta^{\omega}_3). \tag{13}$$

In Fig. 3(a) these field components, labeled (i)–(iv), are plotted as a function of incident angle θ^{ω}_1. In addition, we use a transfer matrix method [25] to map the field across the entire system; see Figs. 3(b) and 3(c). The field magnitude inside the absorbing film increases when θ^{ω}_1 is adjusted to match the LRSEP resonance (b), in comparison to the off-resonant case (c). Note that the field in the cladding, adjoining the Mo film, also increases on resonance, and is about three times as strong in comparison to the interior field.

The fundamental fields drive second-harmonic polarization sheets at these locations [26], which in SI units have the amplitudes

$$P^{2\omega}_{3,x}(z) = \epsilon_0\, \chi^{(2)}_{x:xz}(z)\, E^{\omega}_{3,x}(z)\, E^{\omega}_{3,z}(z), \tag{14}$$

$$P^{2\omega}_{3,z}(z) = \epsilon_0 \left[\chi^{(2)}_{z:xx}(z)\, E^{\omega}_{3,x}(z)\, E^{\omega}_{3,x}(z) + \chi^{(2)}_{z:zz}(z)\, E^{\omega}_{3,z}(z)\, E^{\omega}_{3,z}(z)\right], \tag{15}$$

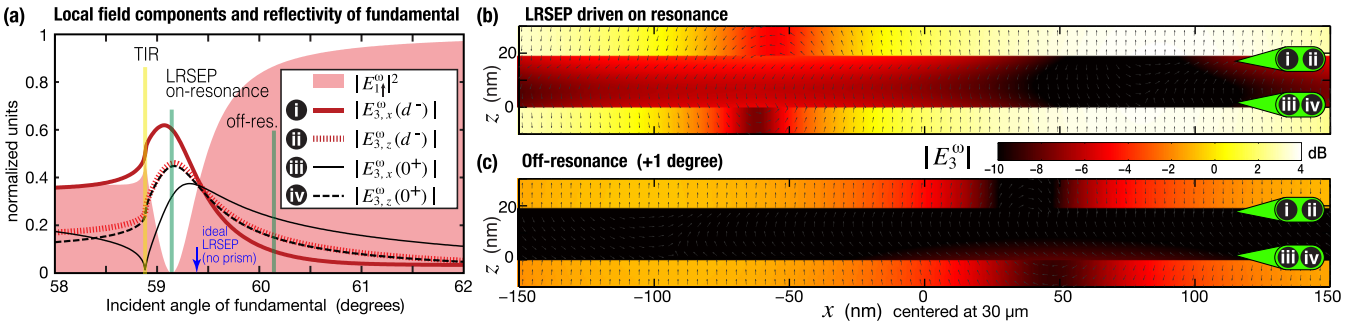

FIG. 3. Analysis of fundamental light (860 nm) in the Mo film for critical coupling (709 nm gap to prism). (a) Intensity reflectivity of the system is plotted (shaded pink curve) as a function of incident angle. Angles beyond the TIR line signify the transition to evanescent fields. The absorption feature confirms that phase matching to the LRSEP mode has been met, i.e., a resonance in momentum space. The electric field is sampled within the film, at locations that are adjacent to the interfaces: red (black) lines for the top (bottom). Solid (dashed) lines refer to the magnitudes of the x- (z-) field components which are normalized to their values in the coupling prism. The LRSEP resonance is concomitant with a field enhancement when compared to the off-resonance case. Panel (b) shows the instantaneous electric-field distribution across the film and its surroundings for the case of LRSEP on resonance (magnitude in dB as a color map). The range plotted covers half a wave cycle. Labels (i)–(iv) mark locations of the component field analysis in (a). (c) The off-resonance case reveals a lower field strength throughout the system.

with ϵ_0 as the permittivity of free space. Due to symmetry arguments for the upper and lower interfaces, one must demand that $\chi^{(2)}_{x:xz}(0^+) = -\chi^{(2)}_{x:xz}(d^-)$, $\chi^{(2)}_{z:xx}(0^+) = -\chi^{(2)}_{z:xx}(d^-)$, and $\chi^{(2)}_{z:zz}(0^+) = -\chi^{(2)}_{z:zz}(d^-)$. Surface sources are difficult to quantify *a priori* because they strongly depend on surface roughness and adsorbed molecules [22]. Our model therefore uses three free parameters, namely, the surface second-order nonlinear coefficients of the Mo film: $\chi^{(2)}_{x:xz}$, $\chi^{(2)\text{eff}}_{z:xx}$, and $\chi^{(2)\text{eff}}_{z:zz}$. These are freely chosen to best fit the experimental data, noting that complex values for surface nonlinear susceptibilities cannot be ruled out [27].

D. Out coupling of the second harmonic

The second-harmonic polarization sheet generates plane waves that exit the prism at the angle $\sin(\theta_1^{2\omega}) = \sin(\theta_1^{\omega})\sqrt{\epsilon_1^{\omega}/\epsilon_1^{2\omega}}$, which satisfies the condition for momentum conservation for the interaction (nonlinear phase matching). The waves undergo multiple reflections and interfere. The out-coupling transmittivity of each source is therefore of great importance.

Proper treatment of the nonlinear surface source propagation entails putting the source in interfacial layers of vacuum (of vanishing thickness) [28], which are defined by the permittivities $\epsilon^{2\omega}_{\frac{2}{3}}(z=d) = \epsilon^{2\omega}_{\frac{3}{4}}(z=0) = 1$, where one should take heed of the pictorial subscript notation. The amplitude transmittivity of SHG radiated from these locations are, for the upward direction,

$$t^{2\omega}_{\frac{2}{3}\uparrow} = \bar{t}^{2\omega}_{\frac{2}{3}1}/\left(1 - \bar{r}^{2\omega}_{\frac{2}{3}1}\bar{r}^{2\omega}_{\frac{2}{3}4}\right), \tag{16}$$

$$t^{2\omega}_{\frac{3}{4}\uparrow} = \bar{t}^{2\omega}_{\frac{3}{4}1}/\left(1 - \bar{r}^{2\omega}_{\frac{3}{4}1}r^{2\omega}_{\frac{3}{4}4}\right), \tag{17}$$

while for the downward direction we have

$$t^{2\omega}_{\frac{2}{3}\downarrow} = t^{2\omega}_{\frac{2}{3}\uparrow}\bar{r}^{2\omega}_{\frac{2}{3}4}, \tag{18}$$

$$t^{2\omega}_{\frac{3}{4}\downarrow} = t^{2\omega}_{\frac{3}{4}\uparrow}r^{2\omega}_{\frac{3}{4}4}. \tag{19}$$

These expressions depend on the nested resonator terms:

$$\bar{r}^{2\omega}_{\frac{2}{3}1} = r^{2\omega}_{\frac{2}{3}2} + \frac{t^{2\omega}_{\frac{2}{3}2}t^{2\omega}_{2\frac{2}{3}}r^{2\omega}_{21}e^{2i\phi^{2\omega}_2}}{1 - r^{2\omega}_{2\frac{2}{3}}r^{2\omega}_{21}e^{2i\phi^{2\omega}_2}}, \tag{20}$$

$$\bar{t}^{2\omega}_{\frac{2}{3}1} = \frac{t^{2\omega}_{\frac{2}{3}2}t^{2\omega}_{21}e^{i\phi^{2\omega}_2}}{1 - r^{2\omega}_{2\frac{2}{3}}r^{2\omega}_{21}e^{2i\phi^{2\omega}_2}}, \tag{21}$$

$$\bar{r}^{2\omega}_{\frac{2}{3}4} = r^{2\omega}_{\frac{2}{3}3} + \frac{t^{2\omega}_{\frac{2}{3}3}t^{2\omega}_{3\frac{2}{3}}r^{2\omega}_{34}e^{2i\phi^{2\omega}_3}}{1 - r^{2\omega}_{3\frac{2}{3}}r^{2\omega}_{34}e^{2i\phi^{2\omega}_3}}, \tag{22}$$

$$\bar{t}^{2\omega}_{\frac{3}{4}1} = \frac{r^{2\omega}_{\frac{3}{4}3}\bar{t}^{2\omega}_{31}e^{i\phi^{2\omega}_3}}{1 - r^{2\omega}_{3\frac{3}{4}}\bar{r}^{2\omega}_{31}e^{2i\phi^{2\omega}_3}}, \tag{23}$$

$$\bar{r}^{2\omega}_{\frac{3}{4}1} = r^{2\omega}_{\frac{3}{4}3} + \frac{t^{2\omega}_{\frac{3}{4}3}t^{2\omega}_{3\frac{3}{4}}\bar{r}^{2\omega}_{31}e^{2i\phi^{2\omega}_3}}{1 - r^{2\omega}_{3\frac{3}{4}}\bar{r}^{2\omega}_{31}e^{2i\phi^{2\omega}_3}}, \tag{24}$$

$$\bar{t}^{2\omega}_{13} = \frac{t^{2\omega}_{12}t^{2\omega}_{23}e^{i\phi^{2\omega}_2}}{1 - r^{2\omega}_{21}r^{2\omega}_{23}e^{2i\phi^{2\omega}_2}}, \tag{25}$$

$$\bar{r}^{2\omega}_{31} = r^{2\omega}_{32} + \frac{t^{2\omega}_{23}t^{2\omega}_{32}r^{2\omega}_{21}e^{2i\phi^{2\omega}_2}}{1 - r^{2\omega}_{23}r^{2\omega}_{21}e^{2i\phi^{2\omega}_2}}. \tag{26}$$

The polarization sheet radiates both upwards and downwards—constructively interfering at the exit angle $\theta_1^{2\omega}$. The escape efficiencies of the second-harmonic radiation, analyzed into its components taken from the interfacial locations, are

$$\eta^{2\omega}_{\frac{2}{3},x} = \left(t^{2\omega}_{\frac{2}{3}\downarrow} - t^{2\omega}_{\frac{2}{3}\uparrow}\right)\cos(\theta^{2\omega}_{\frac{2}{3}}), \tag{27}$$

$$\eta^{2\omega}_{\frac{2}{3},z} = \left(t^{2\omega}_{\frac{2}{3}\downarrow} + t^{2\omega}_{\frac{2}{3}\uparrow}\right)\sin(\theta^{2\omega}_{\frac{2}{3}}), \tag{28}$$

$$\eta^{2\omega}_{\frac{3}{4},x} = \left(t^{2\omega}_{\frac{3}{4}\downarrow} - t^{2\omega}_{\frac{3}{4}\uparrow}\right)\cos(\theta^{2\omega}_{\frac{3}{4}}), \tag{29}$$

$$\eta^{2\omega}_{\frac{3}{4},z} = \left(t^{2\omega}_{\frac{3}{4}\downarrow} + t^{2\omega}_{\frac{3}{4}\uparrow}\right)\sin(\theta^{2\omega}_{\frac{3}{4}}). \tag{30}$$

Using the result [26], the polarization sheet generates a propagating wave with the total field amplitude (in SI units) given by $E^{2\omega}_{1\uparrow} = E^{2\omega}_{t,1\uparrow} + E^{2\omega}_{b,1\uparrow}$, where

$$E^{2\omega}_{t,1\uparrow} = \frac{ik^{2\omega}_{\frac{2}{3}}}{2\epsilon_0 \cos\left(\theta^{2\omega}_{\frac{2}{3}}\right)}\left[\eta^{2\omega}_{\frac{2}{3},x} P^{2\omega}_{3,x}(d^-) + \eta^{2\omega}_{\frac{2}{3},z} P^{2\omega}_{3,z}(d^-)\right], \quad (31)$$

$$E^{2\omega}_{b,1\uparrow} = \frac{ik^{2\omega}_{\frac{3}{4}}}{2\epsilon_0 \cos\left(\theta^{2\omega}_{\frac{3}{4}}\right)}\left[\eta^{2\omega}_{\frac{3}{4},x} P^{2\omega}_{3,x}(0^+) + \eta^{2\omega}_{\frac{3}{4},z} P^{2\omega}_{3,z}(0^+)\right]. \quad (32)$$

Finally, one needs to translate this into an experimental quantity. We define the input parameters: average fundamental power in vacuum $\mathcal{P}^{\omega}_0$; pulse duration τ_{pulse}; repetition time τ_{rep}; laser spot area A. Using SI units throughout, the peak electric field strength of the fundamental becomes

$$E^{\omega}_{1\downarrow} = \left[\left(\mathcal{P}^{\omega}_0 \tau_{\text{rep}}\right)/\left(2\sqrt{\epsilon^{\omega}_1}\epsilon_0 c A \tau_{\text{pulse}}\right)\right]^{1/2}. \quad (33)$$

Accordingly, the second-harmonic power detected (in vacuum) translates to

$$\mathcal{P}^{2\omega}_0 = 2\sqrt{\epsilon^{2\omega}_1}\epsilon_0 c \left|E^{2\omega}_{1\uparrow}\right|^2 A \tau_{\text{pulse}}/(4\tau_{\text{rep}}), \quad (34)$$

where the anticipated effects of pulse shortening and a reduction in spot area due to the SHG process have been taken into account.

The model parameters in summary are fundamental wavelength $\lambda = 860$ nm, Mo film thickness $d = 19$ nm, fundamental permittivities $\epsilon^{\omega}_1 = 3.103$, $\epsilon^{\omega}_2 = 2.274$, $\epsilon^{\omega}_3 = -0.098 + 22.105i$, and $\epsilon^{\omega}_4 = 2.274$, and second-harmonic permittivities $\epsilon^{2\omega}_1 = 3.343$, $\epsilon^{2\omega}_2 = 2.473$, $\epsilon^{2\omega}_3 = -1.855 + 20.42i$, and $\epsilon^{2\omega}_4 = 2.274$. The surface second-order nonlinear susceptibilities for Mo obtained via least-square fitting to the data in Fig. 4(a) are (in SI units of 10^{-18} m^2/V) $\chi^{(2)}_{x:xz} = (-16 + 14i)$, $\chi^{(2)\text{eff}}_{z:zz} = (-1.6)$, and $\chi^{(2)\text{eff}}_{z:xx} = (0.64 + 0.36i)$. The global phase is arbitrary, yet the absolute values and estimated fit uncertainties are (in units of 10^{-18} m^2/V) $|\chi^{(2)}_{x:xz}| = (21 \pm 8)$, $|\chi^{(2)\text{eff}}_{z:zz}| = (1.6 \pm 0.9)$, and $|\chi^{(2)\text{eff}}_{z:xx}| = (0.8 \pm 0.3)$, which are values that are on the order of those found in other metals [23].

III. EXPERIMENTAL METHOD

The sample consisted of a Mo film (19 ± 1 nm thick) sputtered onto a BK7 substrate. Index-matching fluid injected into the gap between the sample and coupling-prism ensured the condition of symmetric transparent cladding; see Fig. 1(a). A glass prism (SF11) was employed to illuminate and detect the presence of the LRSEP mode via the evanescent field obtained for angles beyond the TIR angle; see Fig. 1(b). The size of the gap between the Mo film and the prism was determined using interferometric techniques, and could be held constant. The wavelength of the mode-locked Ti:sapphire laser (200 fs, 76 MHz, 200 μm beam radius) was set to 860 nm. In reflection, filters rejected the remainder of the 160 mW average incident power of the fundamental. The extracted SHG light (430 nm) emitted by the sample was collected by a CCD sensor. A quadratic dependence of SHG power on fundamental input power was confirmed. Our setup allowed θ^{ω}_1 to be scanned over a narrow range, while simultaneously recording the reflected fundamental power and SHG.

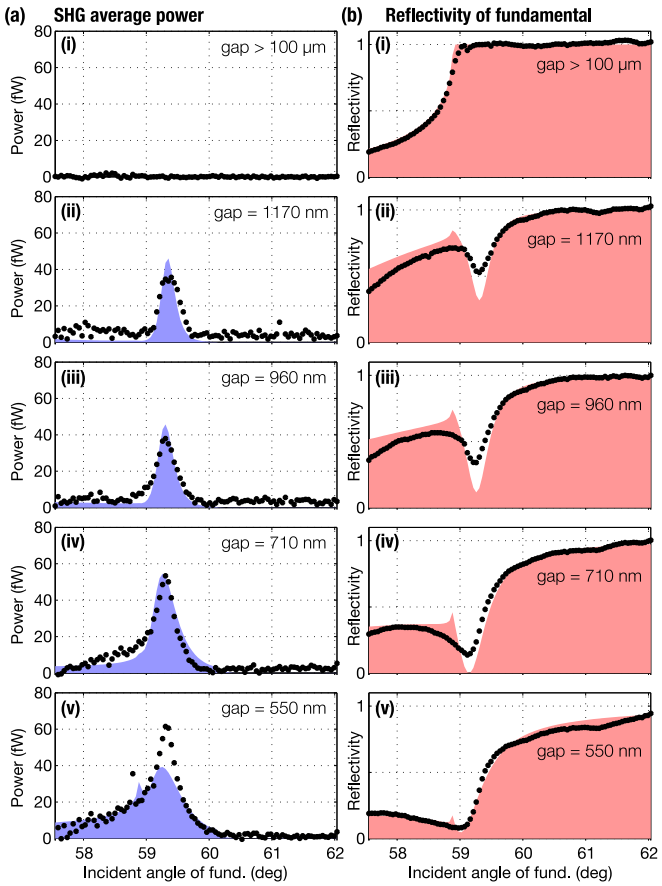

FIG. 4. (a) Experimental results indicate that SHG was driven by excitation of the LRSEP mode which led to a boost in harmonic yield. Average SHG power emitted by the sample is plotted (black dots) over the incident angle of the fundamental driving field. Model calculation (blue shaded curves). A range of separations between the Mo film and the coupling prism were investigated (note gap sizes). (b) Reflectivity of the fundamental shows a narrow absorption feature beyond the angle of TIR which coincides with the SHG peak. Measurements and model calculations are plotted as black dots and red shaded curves, respectively. At large separation (gap > 100 μm) one can see the edge of TIR in the fundamental, while SHG is completely absent due to negligible in- and out-coupling efficiencies. As the prism is moved closer to the film (gap < 1170 nm), coupling to the LRSEP mode improves, which is seen as a strong absorption feature in the fundamental that occurs together with a peak in SHG.

From the measurement in Fig. 4(a)(i), which is essentially of the glass prism and matching fluid alone, we conclude that the overwhelming majority of SHG came from the Mo film. This is supported by measurements of SHG performed in direct reflection (at 45° without a prism), where we could determine an upper bound (via the noise floor) of 0.2% of SHG from the BK7 substrate compared to the Mo film sample.

IV. RESULTS

A peak was observed in the SHG measurements which is consistent with the LRSEP mode having driven the second-order nonlinear interaction; see Fig. 4(a)(ii)–(v). Measurements of ATR of the fundamental in Fig. 4(b)(ii)–(v) revealed

an absorption feature concomitant with the SHG peak, thereby confirming that optical energy was made available to the LRSEP mode. The mode parameters were extracted from ATR data (procedure [21]). The effective LRSEP lifetime (including radiative damping) was thus $N_{\text{eff}} = 106 \pm 11$ wave cycles, which were available for the nonlinear interaction.

Comparing the observed harmonic yield for the resonant and off-resonant cases, one finds (51 ± 2) fW and (2.0 ± 0.7) fW, respectively, which equates to a factor 25 ± 3 boost in measured SHG power; see Fig. 4(a)(iv) at the angles 59.3° and 60.3°. The latter angle was chosen to be distinctly off resonance, yet ensure comparable coupling efficiency. The moderate discrepancy between experiment (black dots) and model (shaded areas) is attributable to a nonzero tilt between sample and prism that hinders ideal critical coupling.

To test whether direct illumination of a film could produce greater harmonic yield than in the prism-coupled case of LRSEP, the model was modified such that the prism was removed: $\epsilon_1^{\omega} \to \epsilon_2^{\omega}$ and $\epsilon_1^{2\omega} \to \epsilon_2^{2\omega}$. Keeping all other parameters constant, the calculated SHG power becomes 3 fW, which is only a fraction of that obtained for the LRSEP case (55 fW). Although a precise comparison of these cases is an experimental challenge, a drop in SHG power of more than two orders of magnitude was observed. These results suggest that the LRSEP mode is active in promoting SHG from the Mo film. The model prediction in Fig. 1(c) shows some potential for increasing SHG yield by reducing the film thickness. However, attention must be given to the fundamental's beam radius (set to 1 mm) to ensure adequate illumination of the LRSEP mode.

V. DISCUSSION

As intrinsic absorption of a material grows its skin depth shrinks, thereby reducing the geometric length scale available for nonlinear interaction. However, by coupling light to the LRSEP mode, one can facilitate an extended interaction due to the mode's propagation lifetime, and also foster an appreciable field enhancement—both of which make the nonlinear yield higher than would otherwise be achievable via direct illumination (no LRSEP) under comparable conditions.

Having understood how LRSEPs increase the yield of a second-order nonlinear process in a centrosymmetric absorber, one can appreciate the potential of LRSEP for enhancing such interactions in noncentrosymmetric absorbers and the extension to third-order nonlinear processes for which nonlinear polarization from the bulk contributes. This makes LRSEP attractive for molecular sensing applications that rely on difference frequency generation or Raman scattering.

In conclusion, our work demonstrates that the LRSEP mode, with its long interaction lifetime and field enhancement properties, is an adept vehicle for utilizing the strong nonlinear susceptibilities that are offered by absorbing materials. As such, we encourage the consideration of absorbing materials as nonlinear media to be employed in optical devices.

ACKNOWLEDGMENTS

This work was supported financially by the Deutsche Forschungsgemeinschaft (DFG) with Grant No. WO 477/35. We thank Robert Franz of Montantuniversität Leoben for preparing the Mo sample.

[1] D. M. Bloom, J. T. Yardley, J. F. Young, and S. E. Harris, Appl. Phys. Lett. **24**, 427 (1974).
[2] D. S. Bethune, R. W. Smith, and Y. R. Shen, Phys. Rev. Lett. **37**, 431 (1976).
[3] D. J. Gauthier, J. Krasinski, and R. W. Boyd, Opt. Lett. **8**, 211 (1983).
[4] J. A. Benda, D. J. Gauthier, and R. W. Boyd, Phys. Rev. A **32**, 3461 (1985).
[5] R. W. Boyd and M. O. Scully, Appl. Phys. Lett. **77**, 3559 (2000).
[6] G. J. Kovacs, J. Opt. Soc. Am. **68**, 1325 (1978).
[7] F. Yang, J. R. Sambles, and G. W. Bradberry, Phys. Rev. Lett. **64**, 559 (1990).
[8] F. Yang, J. R. Sambles, and G. W. Bradberry, Phys. Rev. B **44**, 5855 (1991).
[9] F. Yang, G. W. Bradberry, and J. R. Sambles, J. Mod. Opt. **38**, 565 (1991).
[10] F. Yang, J. R. Sambles, and G. W. Bradberry, J. Mod. Opt. **38**, 707 (1991).
[11] F. Yang, G. W. Bradberry, and J. R. Sambles, Phys. Rev. Lett. **66**, 2030 (1991).
[12] G. P. Bryan-Brown, S. J. Elston, and J. R. Sambles, Thin Solid Films **207**, 252 (1992).
[13] F. Yang and J. R. Sambles, J. Mod. Opt. **39**, 485 (1992).
[14] E. L. Albuquerque and P. Fulco, Phys. Status Solidi B **182**, 357 (1994).
[15] E. L. Wood, J. R. Sambles, F. A. Pudodin, and V. Yakovlev, Opt. Commun. **132**, 212 (1996).
[16] F. Yang and J. R. Sambles, J. Mod. Opt. **44**, 1155 (1997).
[17] V. Giannini, Y. Zhang, M. Forcales, and J. Gómez Rivas, Opt. Express **16**, 19674 (2008).
[18] C. Arnold, Y. Zhang, and J. Gómez Rivas, Appl. Phys. Lett. **96**, 113108 (2010).
[19] C. Arnold, Y. Zhang, and J. Gómez Rivas, Opt. Express **20**, 27554 (2012).
[20] M. Z. Alam, I. De Leon, and R. W. Boyd, Science **352**, 795 (2016).
[21] H. Raether, *Surface Plasmons on Smooth and Rough Surfaces and on Gratings* (Springer, Berlin, 1988).
[22] Y. R. Shen, Annu. Rev. Phys. Chem. **40**, 327 (1989).
[23] F. X. Wang, F. J. Rodríguez, W. M. Albers, R. Ahorinta, J. E. Sipe, and M. Kauranen, Phys. Rev. B **80**, 233402 (2009).
[24] Filmetrics: Sopra Material Database, http//www.filmetrics.com/refractive-index-database/.
[25] E. Fontana and R. H. Pantell, Phys. Rev. B **37**, 3164 (1988).
[26] V. Mizrahi and J. E. Sipe, J. Opt. Soc. Am. B **5**, 660 (1988).
[27] A. Liebsch, Phys. Rev. Lett. **61**, 1233 (1988).
[28] J. Rudnick and E. A. Stern, Phys. Rev. B **4**, 4274 (1971).